



The interaction of a vortex ring with a sloped sediment layer: Critical criteria for incipient grain motion

R. J. Munro

Citation: *Physics of Fluids* **24**, 026604 (2012); doi: 10.1063/1.3683555

View online: <http://dx.doi.org/10.1063/1.3683555>

View Table of Contents: <http://scitation.aip.org/content/aip/journal/pof2/24/2?ver=pdfcov>

Published by the *AIP Publishing*

Articles you may be interested in

[Interaction of a vortex ring with a natural convective layer](#)

Phys. Fluids **26**, 083602 (2014); 10.1063/1.4891985

[Threshold criteria for incipient sediment motion on an inclined bedform in the presence of oscillating-grid turbulence](#)

Phys. Fluids **25**, 015103 (2013); 10.1063/1.4774341

[Resuspension onset and crater erosion by a vortex ring interacting with a particle layer](#)

Phys. Fluids **24**, 063301 (2012); 10.1063/1.4716000

[Sediment resuspension and erosion by vortex rings](#)

Phys. Fluids **21**, 046601 (2009); 10.1063/1.3083318

[Horizontal vortex ring motion in linearly stratified media](#)

Phys. Fluids **9**, 2605 (1997); 10.1063/1.869377

A screenshot of a Google Scholar search results page for the query 'python in scientific computing'. The page shows several search results, including 'Python for scientific computing' by TE Oliphant and 'IPython: a system for interactive scientific computing' by F. Perez, BE. Granger, and J. D. Kowalski. A large green overlay is present on the left and right sides of the image. On the left, it says 'Searching? Trust CiSE.' in a large, bold, black font. On the right, it says 'It's peer-reviewed and appears in the IEEE Xplore and AIP library packages.' in a smaller, black font. The background of the green overlay features a stylized illustration of a city skyline with a large blue sphere in the center, and the text 'NERSC' is visible.

The interaction of a vortex ring with a sloped sediment layer: Critical criteria for incipient grain motion

R. J. Munro^{a)}

Faculty of Engineering, University of Nottingham, Nottingham NG7 2RD, United Kingdom

(Received 23 May 2011; accepted 13 January 2012; published online 14 February 2012)

Experiments were performed to analyse the interaction between a vortex ring and a sloped sediment layer. Attention focussed on interactions under “critical” conditions, in which sediment motion was only just induced by the ring’s flow field. Both hydraulically smooth and hydraulically rough bedforms were analysed, using near-spherical monodisperse sediments with relative densities of 1.2 and 2.5 and mean diameters (d_p) ranging between 80 and 1087 μm . Measurements of the vortex-ring flow field were obtained, during the interaction, using two-dimensional particle imaging velocimetry. The threshold conditions for incipient sediment motion were analysed in terms of the critical Shields parameter (N_c), defined in terms of the peak tangential velocity measured adjacent to the bed surface. Bed-slope effects were investigated by tilting the sediment layer at various angles between the horizontal and the repose limit for the sediment. In all cases, the propagation axis of the vortex ring was aligned normal to the bed surface. The measured values of N_c were compared with a force-balance model based on the conditions for incipient grain motion on a sloping bed. For hydraulically smooth bedforms, where the bed roughness is small compared to the boundary-layer depth, the model was derived to account for how viscous stresses affect the drag and lift forces acting on the near surface sediment. For hydraulically rough bedforms, where this viscous-damping effect is not present, the model assumes the drag and lift forces scale with the square of the near-bed (inviscid) velocity scale. In both cases, the model predicts that bedforms become more mobile as the bed slope is increased. However, the damping effect of the viscous sublayer acts as a stabilizing influence for hydraulically smooth bedforms, to reduce the rate at which the bed mobility increases with bed slope. The measured values of N_c were in agreement with the trends predicted by this model, and exhibit a transition in behaviour between the smooth-bed and rough-bed cases when $d_p/\delta_s \approx 20$ (where δ_s is the viscous-sublayer length scale). © 2012 American Institute of Physics. [<http://dx.doi.org/10.1063/1.3683555>]

I. INTRODUCTION

Methods for predicting bedload sediment-transport rates are largely empirical, and based on measurements taken in steady turbulent channel flows. In such flows, the near-bed turbulent fluctuations, which give rise to the hydrodynamic drag and lift forces that induce sediment motion, are correlated with the time-averaged mean velocity. Hence, the integral parameter used in standard models is the time-averaged mean bed shear stress,^{1–4} with the effects due to turbulent fluctuations considered implicitly. However, in many naturally occurring flows, for which the simplifications of uniformity and stationarity no longer hold, the intensity of turbulent fluctuations in the near-bed region can vary significantly with bed position and time due to factors such as external turbulence generated by flow obstacles,⁵ local bed geometry,^{6,7} or intermittent bursting and ejection events associated with the development of coherent vortex structures within the near bed region.⁸ In such

^{a)}Electronic mail: rick.munro@nottingham.ac.uk. Tel.: +44 (0)115 9513893.

flows, the near-bed turbulence no longer scales with the mean flow characteristics. Indeed, laboratory experiments⁵ have reported up to a factor of six increase in the sediment transport rate for a class of steady open channel flow in which the mean bed shear stress was kept fixed, but with the near-bed turbulence intensity increased by 20% (using an array of grids placed at different heights within the flow). Clearly, clarification of the complex and intermittent turbulence-sediment interaction in the near-bed region is required.⁹

Recent studies have attempted to address some of these issues by analysing the role played by (unsteady) coherent vortex structures in the entrainment and transport of sediments. For example, Munro *et al.*¹⁰ studied sediment erosion induced by an isolated vortex ring interacting with a layer of artificial (transparent) sediment. A light attenuation¹¹ technique was used to obtain detailed time-resolved measurements of sediment erosion levels during the interaction period, and over the entire impact region. It was shown that, during the interaction, the intense vortical flow establishes local regions of high-momentum fluid (or sweeps) immediately above the bed surface which distort (or disrupt) the structure of the boundary layer and inner viscous sublayer. Consequently, the adjacent near-surface sediment is exposed to increased hydrodynamic drag and lift forces. Under the appropriate conditions, the exposed sediment can be displaced along the bed to accumulate in near-by regions of comparatively low-momentum fluid (or bursts), or resuspended into the outer fluid above the bed surface. Niño and García⁸ and Kaftori *et al.*¹² identified analogous behaviour caused by the funnel-shaped streamwise vortices that can develop in the near-bed region of a turbulent channel flow. In this case, the vortical flow induces streaks of high- and low-momentum fluid adjacent to the bed surface, with the displaced sediment forming into narrow, longitudinal troughs and ridges. Each of these studies identified the bed roughness length-scale and the viscous sublayer thickness as the key factors controlling sediment displacement and resuspension.

The fundamental quantity used to describe bedload sediment transport is the dimensionless Shields¹ parameter (N), defined as

$$N = \frac{\sigma_b}{(\rho_p - \rho)d_p g}, \quad (1)$$

where σ_b is a characteristic scale for the bed shear stress, ρ_p and ρ are the sediment and fluid densities, respectively, and d_p is the mean grain diameter. Many predictive formulas^{13,14} for the sediment transport rate are defined in terms of N and the critical Shields parameter, $N_c = \sigma_{b,c}/(\rho_p - \rho)d_p g$, where $\sigma_{b,c}$ is the corresponding critical (or threshold) bed shear stress, below which no sediment movement is induced. Indeed, understanding the conditions under which incipient sediment motion occurs is essential, and so many researchers have focussed attention on studying how N_c depends on sediment size and relative density.^{1-4,15} However, comparatively few studies have analysed how N_c is affected by bed slope (see Lamb *et al.*¹⁶ for a broad overview). Theoretical models¹⁷ predict that a sediment bed becomes more mobile (or unstable) as the bed slope is increased due to the additional down-slope gravitational force. However, some field studies¹⁸ and open-channel experiments¹⁶ have demonstrated the opposite trend that the sediment layer becomes more stable with increasing bed slope. Lamb *et al.*¹⁶ attributes this counter-intuitive result to how the near-bed turbulence in a steady open channel flow is affected by the decrease in flow depth, h , and the corresponding increase in relative roughness, z^*/h , that occurs as the bed slope is increased (where z^* is the roughness length-scale). With this factor eliminated, experimental data exhibit clear agreement with the increased-mobility trend predicted by the theory.^{19,20}

This paper extends the work of Munro *et al.*¹⁰ and describes experiments to investigate how the flow-field of an isolated vortex ring, made to interact with a sediment layer, gives rise to incipient sediment motion. The vortex ring is a simple coherent vortex structure, which can be easily and consistently produced in the laboratory and has been used in a range of previous studies as an idealised model for turbulent entrainment.²¹⁻²³ The vortex ring is used here in a similar context, and is intended to represent an idealised model for the (unsteady) interaction between an isolated eddy and a sediment layer. The focus here was to determine how the critical conditions for incipient sediment motion depend on sediment type (size and relative density) and, in particular, on changes in bed slope between the horizontal and up to the repose limit. One notable advantage of using the vortex ring is that conditions for incipient grain motion could be defined objectively, and determined

with a high degree of repeatability. This is not the case when incipient conditions are studied in turbulent channel flows, where the inherent randomness of the flow inevitably leads to differing (and often subjective) definitions of the threshold conditions, a factor which contributes significantly to the wide scatter observed in experimental data.^{3,16} Note, however, that this study is not intended to be representative of a fully turbulent flow, but to report a detailed set of data that will be useful to theoretical and numerical modellers as a simple test case when developing new models for the turbulence-sediment interaction.

II. EXPERIMENTS

A. Experiment arrangement

A sketch of the apparatus is shown in Fig. 1. Each experiment was performed in an 80 litre acrylic tank containing water. Eleven different monodisperse sediment types were used with a grain density (ρ_p) of 1.2 or 2.5 g/cm³ (Diakon and Ballotini, respectively) and mean grain diameters (d_p) ranging between 80 and 1087 μ m. In each case, the grains were near-spherical with a narrow size distribution about d_p . Table I summarises the properties of the sediment types used, where $C_u = \sqrt{d_{84}/d_{16}}$ is the sediment gradation parameter, w_s is the grain settling velocity (measured in quiescent water), and $Re_p = w_s d_p / \nu$ is the particle Reynolds number (where ν denotes the kinematic viscosity of water).

Each sediment layer was formed in a shallow tray at the base of the tank (see Fig. 1), with the surface of the layer prepared by carefully drawing a straight-edged scraper across the top rim of the tray. This produces a flat, close-packed bed of consistent mean depth 0.5 cm. The bed slope was set by tilting the tray using a threaded depth gauge attached to one side of the tray, and a nut wound up (or down) the gauge to set the required angle ϕ (as shown in Fig. 1). To prevent the sediment bed from sliding on the smooth tray surface when tilted, the tray base was roughened by gluing to its surface a thin layer of type K sediment ($d_p = 1087 \mu$ m). The experiments were performed at a range of bed angles between $0 \leq \phi \leq \phi_r$, where ϕ_r denotes the repose angle for a given sediment type. Each repose angle was determined (in quiescent water) by slowly increasing the bed angle from $\phi = 0$ until the bedform started to become unstable and collapse down the tray. The corresponding measured values of ϕ_r are shown in Table I and are averages taken from several repeats (with typical

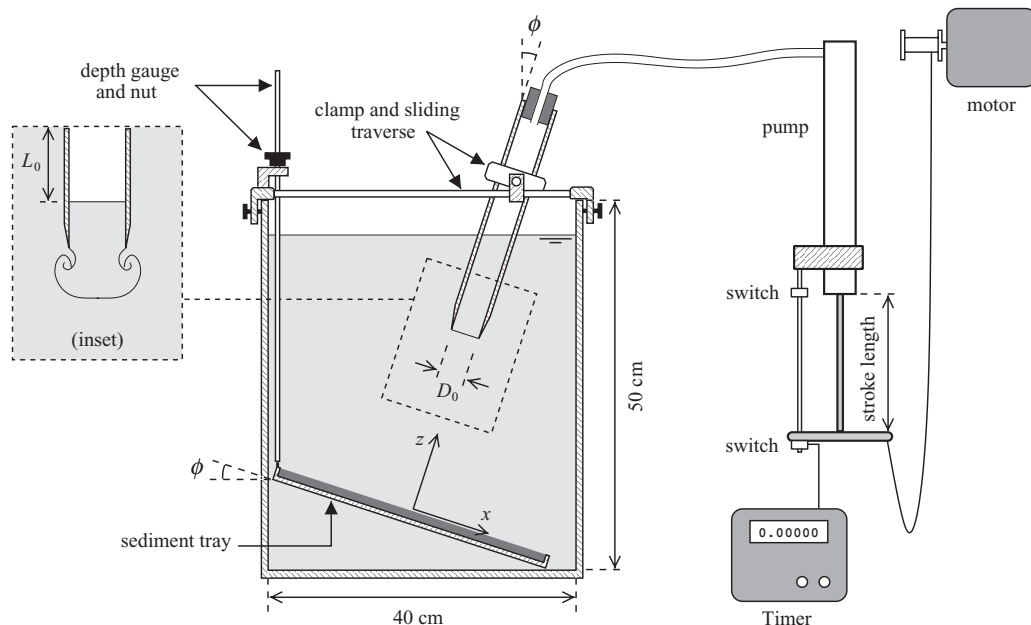


FIG. 1. Sketch of experimental setup.

TABLE I. Properties of the sediment particles, listed in order of increasing grain size (d_p). The †-superscript indicates the sediment types for which sediment velocities were obtained (see text for details).

Label	Type	ρ_p (g/cm ³)	d_p (μ m)	C_u	w_s (cm/s)	Re_p	ϕ_r (deg)
A	Ballotini	2.5	80	1.66	0.870	0.696	24
B	Diakon	1.2	119	1.53	0.390	0.464	26
C	Diakon	1.2	157	1.20	0.420	0.659	27
D	Ballotini	2.5	153	1.32	2.16	3.30	26
E	Ballotini	2.5	220	1.44	3.06	6.73	26
F	Diakon	1.2	274	1.62	0.810	2.22	27
G	Ballotini	2.5	374	1.35	5.06	18.9	26
H	Ballotini	2.5	563	1.30	6.93	39.0	26
I†	Diakon	1.2	751	1.28	2.6	19.8	28
J	Ballotini	2.5	709	1.23	9.20	65.2	28
K†	Ballotini	2.5	1087	1.15	15.2	165.0	29

variability of $\pm 1^\circ$). The corresponding bed slope is henceforth defined as $\beta = \tan \phi$, and $\beta_r = \tan \phi_r$ denotes the bed slope at the repose limit.

Each vortex ring was generated using a uniform cylindrical tube (internal diameter $D_0 = 4$ cm, length = 40 cm) clamped in position above the tank with the outlet submerged below the water free-surface (see Fig. 1). The tube inlet was sealed with an air-tight fitting and connected to a cycle track pump by a length of hose. Actuation of the pump caused the air cavity inside the tube to expand, forcing a pre-determined volume of water from the tube outlet. As the fluid “slug” exits the tube, the vortex sheet shed at the lip of the outlet rolled up to form the vortex ring²⁴ (see inset of Fig. 1). Once fully formed, each vortex ring propagated away from the outlet along the central symmetry axis of the tube, until interacting with the sediment layer. In all experiments reported here, the central propagation axis of each vortex ring was aligned to be perpendicular to the planar bed surface. This ensured that the basic characteristics of the ring flow field (for both horizontal and sloped beds) were essentially axisymmetric at the point of impact. Hence, an adjustable clamp and traverse mechanism was used to tilt and hold the tube at the corresponding angle ϕ to the vertical (as shown in Fig. 1).

Once fully formed, each vortex ring travelled a relatively short distance (approximately $5D_0 = 20$ cm) before the ring structure and trajectory were noticeably affected by the presence of the sediment layer, which occurred when the core of the ring had reached a height of approximately $D_0/2$ above the bed surface.¹⁰ Over this short distance, very little ambient, irrotational fluid is entrained within the ring structure (by diffusion).^{21,24} Hence, prior to being affected by the presence of the sediment layer, the ring diameter (D) and axial propagation speed (U) were essentially constant. [Here, D is defined as the diameter of the ring core, as illustrated in Fig. 5(a).]

The important characteristics of each vortex ring (namely, D and U) were determined by the tube diameter, $D_0 = 4$ cm, and the stroke length and stroke time of the pump (see Fig. 1).¹⁰ For the experiments described here, a fixed stroke length of 20 cm was used throughout, which produced a fluid slug of length $L_0 = 9.5$ cm (i.e., $L_0/D_0 = 2.4$). The pump actuation rate was controlled by attaching the pump handle to a motor-driven spool by a length of nylon cord (see Fig. 1). The pump stroke time was controlled by adjusting the rotation rate of the motor and measured using a digital timer connected to two switches positioned to detect the start and end of the pump stroke (see Fig. 1). With this system, the ring diameter D and, most importantly, the propagation speed U were controlled by adjusting the pump stroke time.^{10,25} [For the experiments reported here, the measured stroke times were within the range 0.1–0.9 s.]

For a given sediment type and bed slope (β), the critical conditions for incipient motion were determined by repeating an experiment, each time systematically increasing the pump stroke time (thereby decreasing U) until grain motion was only just observed to occur, with any further increase in stroke time resulting in no motion. During this procedure, the sediment layer was re-scraped

and made flat prior to each repeat. Once the appropriate stroke time for critical conditions had been identified, the velocity field of the corresponding vortex ring was measured using particle imaging velocimetry (PIV), the details of which are given below in Sec. II B. Note that the PIV data captured the ring flow-field over the entire impact region, and at each stage during the interaction. To minimise the experimental errors associated with the incremental increase of the pump stroke time, the entire procedure described above was repeated several times (for each sediment type and bed slope) so that an average could be taken. The velocity data were also used to directly measure U and D for each vortex ring (from the period before the ring's trajectory was affected by the sediment layer). The values of U and D reported here are the corresponding averages obtained from the repeated experiments, which had typical variability of $\pm 6\%$ and $\pm 4\%$, respectively. Over the range of critical impact conditions analysed in this article, the corresponding vortex ring Reynolds number, $Re = UD/\nu$, was varied between 450 and 3360 (where $0.8 \leq D/D_0 \leq 1.2$).

The standard PIV technique was also adapted to measure the velocity field of the displaced sediment grains (within the transverse plane of the bed surface) during the impact period. Details of this method are given below in Sec. II C. Note that, for impacts close to critical conditions (i.e., $1 \leq N/N_c \lesssim 2$), grain motion is only just induced by the interaction. Hence, to ensure that a noticeable level of sediment motion could be detected, the sediment PIV experiments were performed for $5 \leq N/N_c \leq 8$. Furthermore, for the experiments reported here, it was found that this technique could only be applied to the larger sediment types with $d_p \gtrsim 700 \mu\text{m}$ (the reasons for which are discussed below in Sec. II C). These restrictions precluded using the sediment velocity data for an in-depth parametric analysis. Hence, since the focus here was to measure the critical conditions for incipient grain motion, the sediment PIV technique was used only to provide novel data to illustrate the basic impact characteristics. For this reason, the sediment PIV technique was applied only to the case of horizontal bedforms ($\beta = 0$).

B. Fluid PIV measurements

The vortex ring velocity fields were obtained using two-dimensional planar PIV. Small neutrally buoyant tracer particles were added to the water volume, and a narrow vertical light sheet (of approximate thickness 2 mm) used to illuminate the seeding particles within the vertical midplane of the vortex ring trajectory. The motion of the tracer particles was recorded using a high-speed Dantec Nanosense MkIII digital camera (with 1280×1024 pixel resolution and frame rate set at 600 Hz), positioned to view horizontally through the transparent sidewall of the tank (corresponding to the view shown in Fig. 1). For the sloping beds, the camera was tilted on its side, at the angle ϕ , so that the surface of the sediment layer appeared horizontal at the base of each image. The velocity fields were calculated directly from the captured images using the PIV algorithm within Digiflow.²⁶ Images were recorded throughout the interaction period, but also during the period prior to impact so that U and D could be determined. [The setup described above will be referred to below as PIV setup 1.]

C. Sediment PIV measurements

The sediment velocity data were obtained using a simple adaptation of the standard PIV technique. In this case, a random pattern structure was established within the bed using black sediment grains added to, and mixed thoroughly with, the otherwise transparent sediment. When the sediment layer was formed in the tray and illuminated by a halogen spot light, the black opaque grains acted as tracer particles within the regular sediment. Images of two seeded sediment layers produced in this way (prior to impact) are shown in Fig. 2. In each case, the basic properties of the black particles (d_p and Re_p) were the same as those for the corresponding regular sediment. Best results were obtained using a particle mixture ratio of about 30% black to 70% transparent.

The high-speed Nanosense camera (with frame rate set at 600 Hz) was positioned above the tank and aligned to view down onto the layer surface at an angle close to the vertical, so that the tube used to generate the vortex ring did not obstruct the camera view. A transparent acrylic lid was placed across the water surface to eliminate distortion effects due to free-surface displacements. As the vortex ring

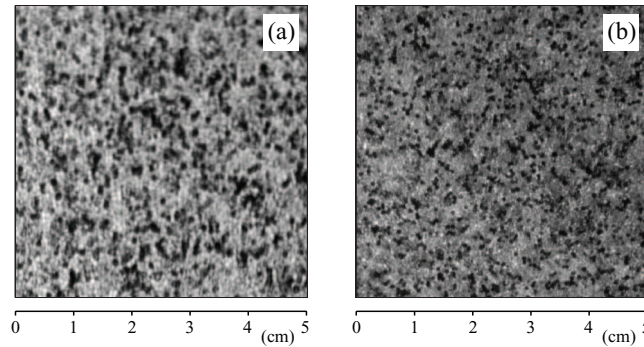


FIG. 2. Images showing two different layers of mixed black and transparent particles: (a) Ballotini with $d_p = 1087 \mu\text{m}$ (type K) and (b) Diakon with $d_p = 751 \mu\text{m}$ (type I). In both images, the mixture ratio is 30% black, 70% transparent, and the region shown corresponds to an area of $5 \times 5 \text{ cm}^2$ on the bed surface.

interacted with and displaced the near-surface sediment, the motion and trajectories of the tracer grains (within the plane of the bed surface) were captured in the images. The corresponding velocity fields were obtained by applying the Digiflow PIV algorithm²⁶ directly to the images. Note that, an energetic interaction could result in a significant number of sediment grains being resuspended above the impact region,¹⁰ which obstructed the camera view and affected the velocity measurements. For this reason, attention was restricted to impacts with $5 \leq N/N_c \leq 8$.

Note that it was necessary for the images to capture the motion of the sediment grains over the entire impact region. To facilitate this, the high-speed camera had to be positioned between 60 and 70 cm vertically above the sediment layer surface. However, at this height the motion of only the larger sediment types could be adequately resolved in the captured images, and so, application of the sediment PIV technique was restricted to sediments with $d_p \gtrsim 700 \mu\text{m}$. The data reported here are for sediment types I and K. [Recall, attention was also restricted to horizontal beds, $\beta = 0$.]

The controllable pump mechanism meant that each vortex ring could be generated with a high degree of repeatability. Hence, each sediment-velocity experiment was repeated (using PIV setup 1) so that corresponding fluid velocity data could be obtained and compared with the sediment velocity data. Care was taken to ensure that the conditions of each experiment were near-identical in each case. These data are used (in Sec. III A) to illustrate the key characteristics of the interactions.

D. Velocity data

The fluid and sediment velocity fields were obtained in terms of the right-handed Cartesian coordinates (x, y, z) , defined with the (x, y) -axes in the transverse plane of the bed and the positive z -axis directed normal to the bed surface (see Fig. 1). [Let \hat{x} , \hat{y} , \hat{z} denote the unit vectors in the axial directions.] Figures 3(a)–3(c) show a typical sequence of mid-plane fluid velocity fields, denoted by $u(x, z, t)\hat{x} + w(x, z, t)\hat{z}$, obtained during a typical impact (see caption for details). Corresponding dimensionless times are shown at the top of each figure, where $\tau = D/2U$ is the vortex-ring time scale.¹⁰ Figures 3(d)–3(f) show the corresponding sequence of sediment velocity fields, denoted by $u_p(x, y, t)\hat{x} + v_p(x, y, t)\hat{y}$, obtained under the same interaction conditions and at corresponding times during the impact.

To prevent data saturation, only every fifth velocity vector has been included in each of the velocity fields shown in Fig. 3. Furthermore, over the time interval shown (a period of 0.153 s), more than 90 samples of both the fluid and sediment velocity fields were captured. Also note that t_1 is used in Fig. 3 to denote the time at which the vortex ring is located at a height $z = D/2$ above the bed surface, and it is after this time that the ring structure is noticeably affected by the presence of the sediment layer. [That is, the presence of the boundary acts to slow the rate of approach toward the layer surface, and to increase the ring diameter, thus stretching the vortex.¹⁰] However, fluid velocity data were also captured at earlier times with the ring located further from the bed surface

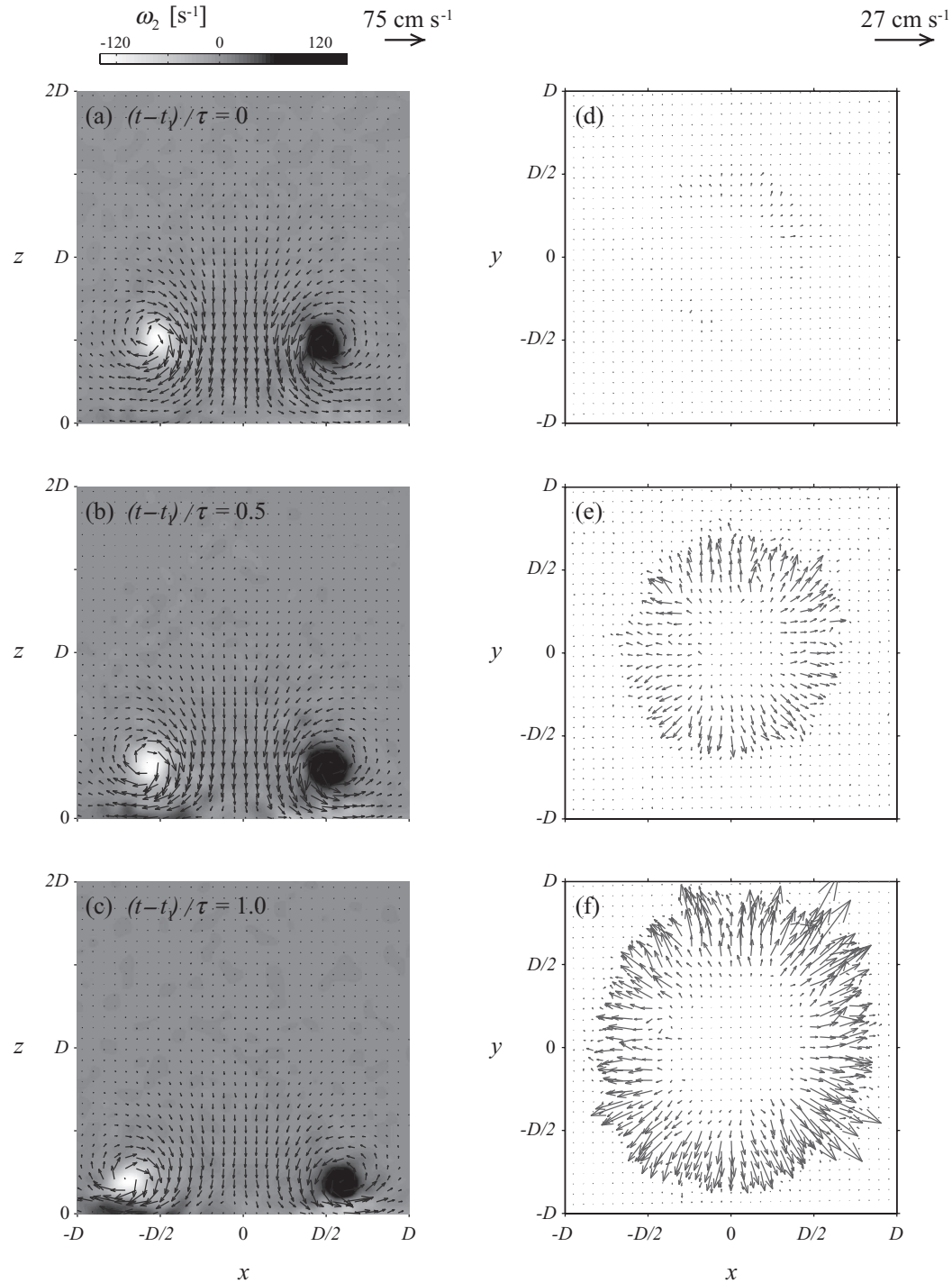


FIG. 3. Sequences of measured fluid velocity fields [(a)–(c)] and corresponding sediment velocities [(d)–(f)] obtained at corresponding dimensionless times during the interaction. The impact shown corresponds to a vortex ring (with $N/N_c = 7.95$, $Re = 11\,100$, and $D = 5.83 \text{ cm}$) interacting with a sediment layer of type K (with $\beta = 0$). Dimensionless times are shown at the top of (a)–(c), where $\tau = D/2U = 0.153 \text{ s}$ is the vortex-ring time scale and t_1 is the time at which the ring is located at height $z = D/2$ above the bed surface. The velocity scales and monochrome vorticity scale for $\omega_2 = (\partial u/\partial z - \partial w/\partial x)$ are shown above the respective plots.

(between $z/D \approx 1$ and 2). During these times the ring moves with near-constant propagation speed and diameter, and it is from this period that D and U were measured.

Recall that, for all bed slopes $0 \leq \beta \leq \beta_r$, the propagation axis of each vortex ring was aligned to be perpendicular to the bed surface, thus ensuring that the ring flow field at the point of impact was essentially axisymmetric. However, when $\beta > 0$, the sediment grains are exposed to a non-zero component of gravitational acceleration acting in the downslope direction. Consequently, the induced sediment-velocity fields are axisymmetric in nature only when $\beta = 0$ (see Figs. 3(d)–3(f)). The overall axisymmetric nature of the interaction (for $\beta = 0$) suggests that the sediment velocity data presented here are best analysed in terms of polar coordinates (r, θ) , where as usual, $x = r \cos \theta$ and $y = r \sin \theta$. With $x = 0$, $y = 0$ aligned with centre of the impact region (see Fig. 3), the sediment velocity components (u_p, v_p) were converted into corresponding polar form using the transformation

$$u_{r,p} = u_p \cos \theta + v_p \sin \theta, \quad (2a)$$

$$u_{\theta,p} = -u_p \sin \theta + v_p \cos \theta, \quad (2b)$$

where $u_{r,p}(r, \theta, t)$ and $u_{\theta,p}(r, \theta, t)$ denote, respectively, the radial and azimuthal components of sediment velocity. Furthermore, in anticipation of the data presented in Sec. III A, it is convenient at this point to introduce the (azimuthally averaged) mean velocity components, defined as

$$\langle u_{r,p} \rangle(r, t) = \frac{1}{2\pi} \int_0^{2\pi} u_{r,p}(r, \theta, t) d\theta, \quad (3a)$$

$$\langle u_{\theta,p} \rangle(r, t) = \frac{1}{2\pi} \int_0^{2\pi} u_{\theta,p}(r, \theta, t) d\theta. \quad (3b)$$

Figure 4 shows the $\langle u_{r,p} \rangle$ and $\langle u_{\theta,p} \rangle$ (solid lines) obtained by applying Eq. (3) to the sediment velocity data in Fig. 3(f). Also shown (broken lines) are the bounds within which the corresponding values of $u_{r,p}$ and $u_{\theta,p}$ were contained.

The non-zero components of $u_{\theta,p}(r, \theta, t)$ [illustrated by the broken-line curves shown in Fig. 4(b)] are caused, primarily, by an azimuthal instability in the form of a sinusoidal perturbation of the ring core,^{27,28} that can develop as the vortex ring propagates through the fluid. During the interaction, the instability gives rise to azimuthal components of fluid velocity adjacent to the

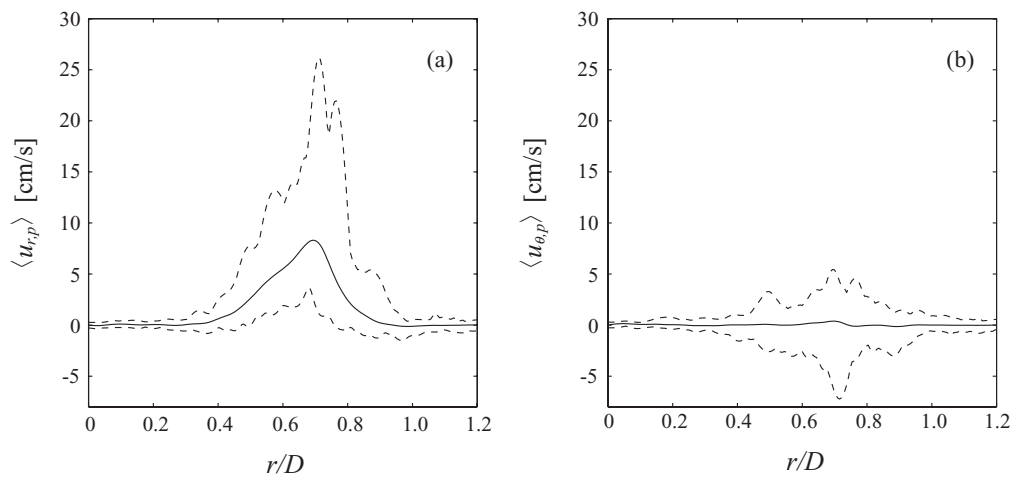


FIG. 4. (a) and (b) The solid lines show the mean velocity profiles $\langle u_{r,p} \rangle$ and $\langle u_{\theta,p} \rangle$, plotted against dimensionless radius r/D , and calculated using Eq. (3) applied to the sediment velocity data $(u_{r,p}, u_{\theta,p})$ taken from Fig. 3(f) [at time $(t - t_1)/\tau = 1$]. The broken lines show the corresponding bounds within which the respective values of $u_{r,p}$ and $u_{\theta,p}$ were contained.

bed surface, which in turn induce azimuthal velocity of the sediment grains and cause spoke-like scar patterns to form around the surface of the impact crater. [A detailed discussion and illustration of these scar features is given in Munro *et al.*¹⁰ – see Sec. III B and Figs. 7–9 of that paper.] However, note that the magnitude of the local azimuthal components of fluid velocity arising due to the instability are always small compared to the corresponding radial component.²⁷ Therefore, under critical impact conditions, and for both horizontal and sloped bedforms, it is the dominant radial fluid velocity component that acts to induce incipient grain motion.

III. RESULTS

The Shields parameter was defined in Sec. I: $N = \sigma_b / (\rho_p - \rho) d_p g$. For a steady turbulent channel flow, estimation of the bed shear stress σ_b is standard. [For example, $\sigma_b = \rho u_*^2$, where u_* is the bed shear velocity, which for a shallow-sloped channel is given by $u_* = \sqrt{g R_h S}$, where R_h and S denote the hydraulic radius and channel gradient, respectively.³] For the experiments described in this article, the boundary layer induced by the interaction evolves spatially and with time. Moreover, the velocity profile within this region is not known, with previous studies being exclusive to a vortex ring interacting with solid (non-porous) surfaces, with axisymmetry assumed and for values of Re notably smaller than those considered here.^{29,30} Hence, an analogous standard parameterisation was not possible and an alternative estimate for σ_b was required, based on the available fluid velocity data. The following approach was adopted.

Let $u_b(x, t)$ denote the horizontal fluid velocity component measured above the bed surface at height $z_b = 0.2$ cm [i.e., $u_b(x, t) = u(x, z_b, t)$], which is as close to the bed surface at which reliable velocity measurements could be consistently obtained using PIV setup 1 (described in Sec. II B). For an impact under critical conditions, the sediment grains are only just brought into motion, and this motion is caused by the *peak* value attained by the induced bed shear stress during the impact. We expect this peak bed shear stress to scale with $\rho \hat{u}_b^2$, where \hat{u}_b denotes the maximum (or peak) value of $u_b(x, t)$ attained during the interaction period. [It will be shown subsequently (using Figs. 6–8) that, during an interaction, the instantaneous peak values of $u_b(x, t)$ occur directly below the vortex ring core, with the overall peak value (\hat{u}_b) attained at time $(t - t_1)/\tau \approx 1$, which corresponds to when the ring core is at its closest point to the bed surface.] Hence, in the present context, using $\sigma_b \sim \rho \hat{u}_b^2$ in Eq. (1), the Shields parameter was defined as

$$N = \frac{\hat{u}_b^2}{(s - 1) d_p g}, \quad (4)$$

where $s = \rho_p / \rho$ is the relative density of the sediment. The corresponding critical Shields parameter is given by

$$N_c = \frac{\hat{u}_{b,c}^2}{(s - 1) d_p g}, \quad (5)$$

where $\hat{u}_{b,c}$ denotes the value of \hat{u}_b measured under critical impact conditions. As already noted, for a steady turbulent channel flow σ_b is defined in terms of a velocity scale based on the time-averaged mean velocity. The approach adopted here uses a velocity scale characteristic of the peak variation in the time-dependent near-bed velocity during the interaction period.

A. Interaction characteristics

Before the measured values of N_c are presented, the interaction characteristics are described and illustrated. Several of the key features discussed here are similar to those observed when a vortex ring interacts with a solid-wall boundary, which has been studied previously by Walker *et al.*,²⁹ and related articles.^{30,31}

Figure 5 shows a sequence of images taken at different stages during a typical impact (see caption for details). Here, the internal structure of the vortex ring has been made visible using fluorescent dye and a vertical light sheet to illuminate the mid-plane of the ring's trajectory. Corresponding

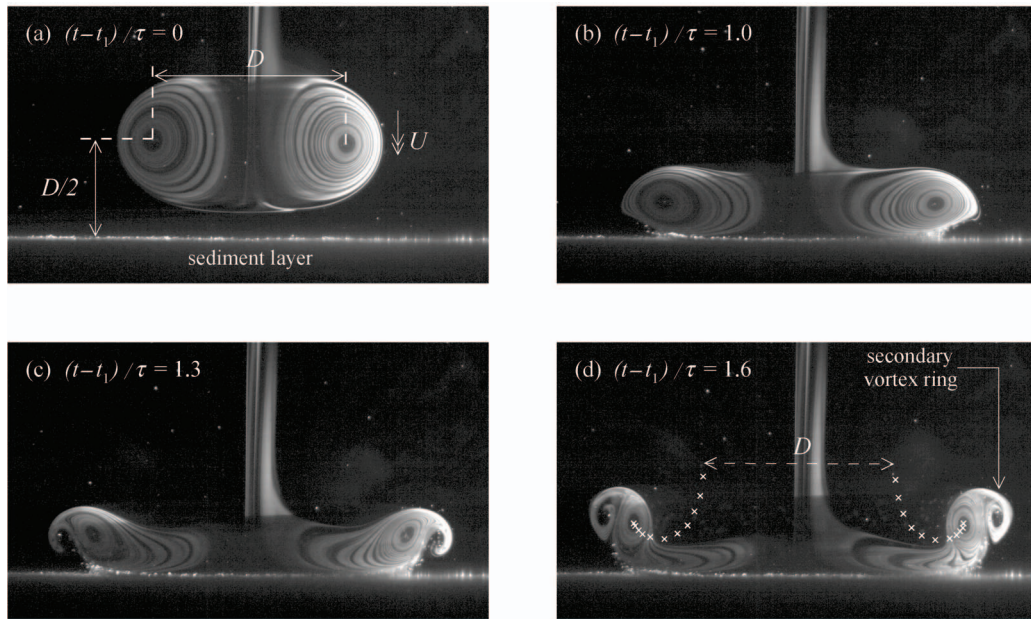


FIG. 5. (a)–(d) A sequence of images showing different stages of an impact using type G sediment, with $N/N_c = 3.45$, $Re = 5700$, $D = 5.0$ cm, $\tau = D/2U = 0.231$ s, and $\beta = 0$. Corresponding dimensionless times are given at the top of each frame. In (d), white crosses have been included to show the trajectory of the ring core, with the first pair showing the core positions at $(t - t_1)/\tau = 0$. The pair of crosses closest to the layer surface corresponds to $(t - t_1)/\tau \approx 1$. [These images are taken from Munro *et al.*¹⁰]

dimensionless times are shown at the top of each frame. Once fully formed, the vortex ring propagates towards the sediment layer with near-constant diameter (D) and speed (U). However, when the ring core reaches a height $z = D/2$ above the layer surface (Fig. 5(a)), the structure and trajectory of the vortex ring are thereafter noticeably altered by the presence of the layer.²⁹ That is, the velocity field induced by the ring's image in the boundary acts to slow its rate of approach towards the layer surface and to increase the ring's diameter (Figs. 5(b)–5(d)), resulting in an increase in peak vorticity within the ring core (but with circulation conserved). In the hypothetical inviscid case ($\nu = 0$), the ring diameter would increase indefinitely, with the core positions gradually moving closer to the boundary.³¹ However, the observed behaviour (for $\nu \neq 0$) is notably different from this, as illustrated by Fig. 5(d), where the white crosses have been included to show the trajectory of the ring core during this period of the impact. That is, the ring diameter increases but attains a maximum, and the vortex core is seen to rebound from the layer surface during the interaction.

Walker *et al.*²⁹ showed that the observed behaviour is a result of how the unsteady boundary layer adjacent to the bed surface develops, grows, and eventually interacts with the inviscid outer flow. That is, the (approximate) no-slip condition at the bed surface induces vorticity of the opposite sign within the boundary layer. This vorticity separates and, provided Re is sufficiently large (Walker *et al.*²⁹ suggest that $Re \gtrsim 250$), is ejected into the outer inviscid flow region as a secondary vortex ring, which then interacts with the flow field of the original (or primary) vortex ring. The ejection of the secondary ring causes the primary ring to rebound away from the layer surface, with the opposite-sense vorticity of the secondary acting to slow (and eventually limit) the outward radial motion of the primary ring core.²⁹ In Fig. 5, the ejected secondary vortex ring, which initially contains no dye, is first seen at $(t - t_1)/\tau = 1$ deforming the outer streamlines of the primary ring. In subsequent frames (Figs. 5(c) and 5(d)), the secondary ring is clearly visible as it orbits around the perimeter of the primary ring and dye becomes entrained within its structure. The secondary ring continues to orbit the primary, eventually passing over and into the central region of the primary ring where its structure is compressed, causing it to break down. Shortly after this, for $(t - t_1)/\tau \gtrsim 2$, the

structure of the primary ring also breaks down, forming a local patch of turbulence which decays and dissipates the vorticity.

The fluid and sediment velocity data (described in Sec. II) are now compared and used to illustrate how the vortex-ring velocity field interacts with and displaces the near-surface sediment grains. The data for two specific impacts are presented: $N/N_c = 5.92$ (type I, with $s = 1.2$) and $N/N_c = 7.95$ (type K, with $s = 2.5$). Recall that, in both cases $\beta = 0$. Samples of the sediment velocity data for $N/N_c = 7.95$ have been shown previously in Figs. 3 and 4, and will be referred to again below.

For each impact, the (Cartesian) near-bed fluid velocity components $u_b(x, t)$ and $w_b(x, t)$ [where $w_b(x, t) = w(x, z_b, t)$] are compared with the corresponding (azimuthally averaged) radial sediment velocity, $\langle u_{r,p} \rangle(r, t)$, at each time during the impact. [Recall that $\langle u_{\theta,p} \rangle(r, t) \approx 0$ throughout the interaction and has been ignored.] To best facilitate this comparison, the measured values of $u_b(x, t)$ over the ranges $x < 0$ and $x \geq 0$ were used to estimate the corresponding near-bed radial velocity component, henceforth denoted by $\bar{u}_b(r, t)$. [That is, $\bar{u}_b = (u_b^+ + |u_b^-|)/2$, where $u_b^+(x, t)$ and $u_b^-(x, t)$ denote, respectively, the values of $u_b(x, t)$ for $x \geq 0$ and $x < 0$.] Likewise, the same procedure was applied to $w_b(x, t)$ to obtain $\bar{w}_b(r, t)$. Typical examples of $\bar{u}_b(r, t)$, $\bar{w}_b(r, t)$, and $\langle u_{r,p} \rangle(r, t)$, at different times during the interaction, are shown in Figs. 6 (for $N/N_c = 5.92$) and 7 (for $N/N_c = 7.95$), plotted against dimensionless radius r/D . Each velocity profile has been made dimensionless using $\hat{u}_{b,c}$ (which are given in the figure captions). Recall that the values of $\hat{u}_{b,c}$ reported here were obtained from the experiments performed under critical impact conditions. Dimensionless times are given at the top of each plot, and correspond to those shown in Fig. 3.

Each set of fluid and sediment velocity data was obtained from separate experiments, and so a suitable method to first align $\bar{u}_b(r, t)$ and $\bar{w}_b(r, t)$ with $\langle u_{r,p} \rangle(r, t)$, in time, was required. Results from a previous study (of sediment erosion by vortex rings)¹⁰ showed that the maximum level of sediment displacement always occurs at the radial location directly below the (stretching) ring core, corresponding to where $\bar{u}_b(r, t)$ attains its instantaneous maximum value. Moreover, it was shown that onset of grain motion (for $5 \leq N/N_c \leq 8$) is consistently observed to first occur when the ring core is located at height $z/D \approx 0.5$ [i.e., at time $(t - t_1)/\tau \approx 0$].¹⁰ Hence, using these properties, the following alignment procedure was adopted.

The fluid velocity profile $\bar{u}_b(r, t)$, at time $(t - t_1)/\tau = 1$, was selected as a reference profile (a time at which significant sediment motion had been induced). The corresponding sediment velocity profile, $\langle u_{r,p} \rangle(r, t)$, was then identified so that the peak values of \bar{u}_b and $\langle u_{r,p} \rangle$ were aligned at (approximately) the same radial location *and* so that the (spatial) correlation between \bar{u}_b and $\langle u_{r,p} \rangle$ was maximised. The remaining data were then aligned relative to these two profiles, noting that each pair of data was obtained at the same frame rate (600 Hz). Once the alignment procedure had been applied, two additional checks were made. First, that the maximum values of $\langle u_{r,p} \rangle(r, t)$ and $\bar{u}_b(r, t)$ remained radially aligned throughout the interaction period, and second, by tracking back in time through each paired set of profiles to ensure that initial sediment motion occurred at $(t - t_1)/\tau \approx 0$. These two conditions were satisfied by the data for both impacts, as illustrated by the aligned profiles shown in Figs. 6 and 7,

Figures 6 and 7 show the period $0 \leq (t - t_1)/\tau \leq 1$, during which the ring is stretched by the presence of the bed, but the ring core continues to approach the bed surface (as illustrated previously in Fig. 5). As already noted, the vortical flow of the ring induces a bed shear stress that scales with $\rho \bar{u}_b^2(r, t)$, and which consistently attains a maximum value directly below the ring core, throughout the interaction. When the ring is located far above the bed, $\bar{u}_b(r, t) \approx 0$. As the outer streamlines of the vortex ring approach the bed surface, the magnitude of $\bar{u}_b(r, t)$ increases and sediment motion is induced only when (and at bed locations for which) $\bar{u}_b(r, t)$ exceeds the threshold value $\hat{u}_{b,c}$. In Figs. 6 and 7, this first occurs below the ring core ($r/D \approx 0.5$) and at time $(t - t_1)/\tau \approx 0$ (i.e., when the ring core is located at height $z/D \approx 0.5$ above the bed). For $0 \leq (t - t_1)/\tau \leq 1$, $\bar{u}_b(r, t)$ continues to increase uniformly as the ring core and outer streamlines move closer to the bed surface. The corresponding increase in bed shear stress means that sediment motion is induced over the annular region (best illustrated by Figs. 3(e) and 3(f) for which the threshold condition $\bar{u}_b/\hat{u}_{b,c} \geq 1$ is satisfied (identified in Figs. 6 and 7 by the thin dotted lines). Moreover, the radius of this annular region increases as the stretched ring diameter increases (see Fig. 3). The instantaneous peak values

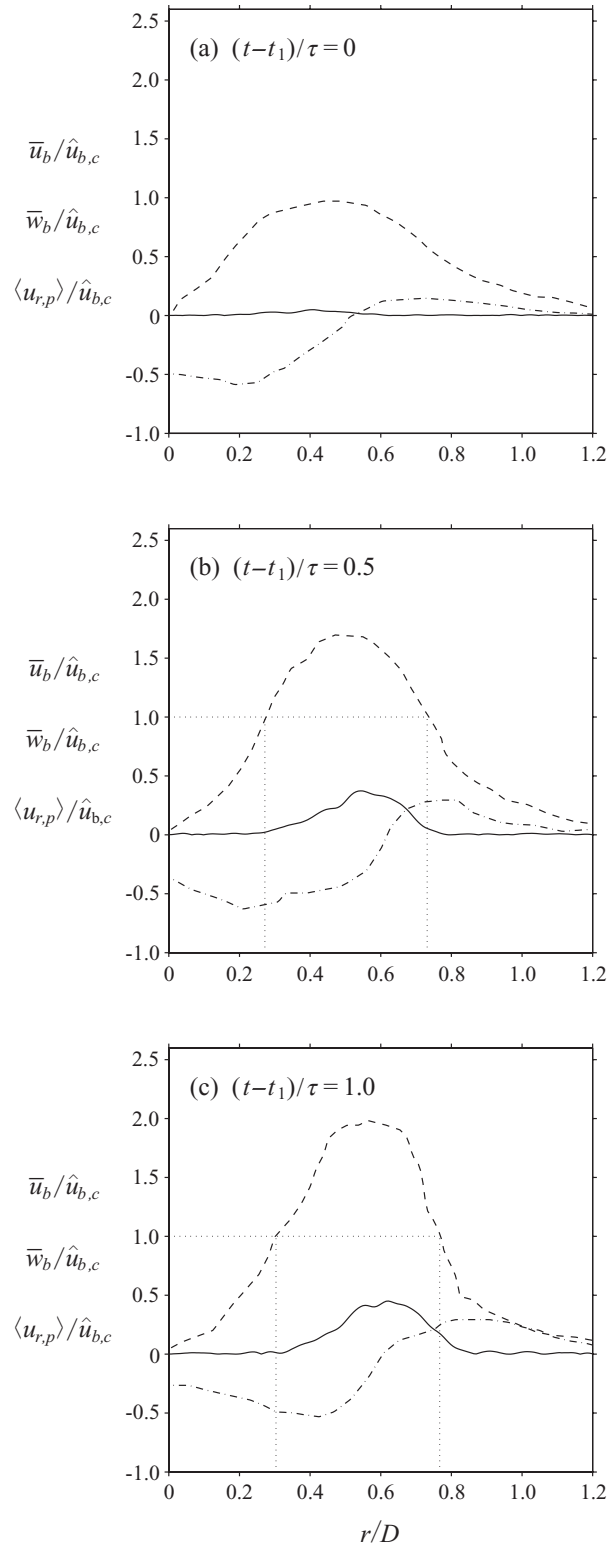


FIG. 6. (a)–(c) Measured values of $\bar{u}_b/\hat{u}_{b,c}$ (broken line), $\bar{w}_b/\hat{u}_{b,c}$ (dashed–dotted line), and $\langle u_{r,p} \rangle/\hat{u}_{b,c}$ (solid line) plotted against r/D at various dimensionless times, $(t-t_1)/\tau$ (as shown), during the impact. This impact corresponds to type I sediment with $N/N_c = 5.92$, $\beta = 0$, and $\hat{u}_{b,c} = 4.31$ cm/s (with ring characteristics $D = 5.38$ cm, $Re = 3020$, and $\tau = 0.479$ s). The dotted lines indicate the radial region for which the threshold condition $\bar{u}_b/\hat{u}_{b,c} \geq 1$ is satisfied.

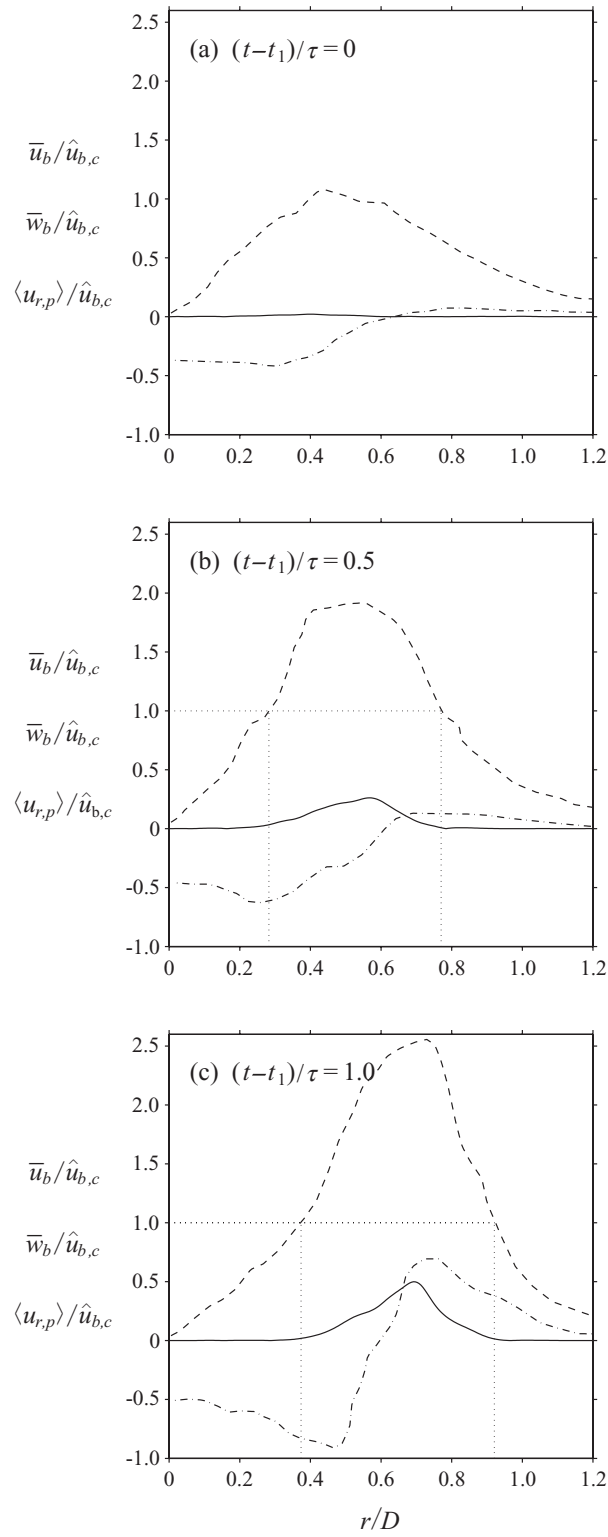


FIG. 7. (a)–(c) Measured values of $\bar{u}_b/\hat{u}_{b,c}$ (broken line), $\bar{w}_b/\hat{u}_{b,c}$ (dashed–dotted line), and $\langle u_{r,p} \rangle/\hat{u}_{b,c}$ (solid line) plotted against r/D at various dimensionless times, $(t - t_1)/\tau$ (as shown), during the impact. This impact corresponds to type K sediment with $N/N_c = 7.95$, $\beta = 0$, and $\hat{u}_{b,c} = 15.3$ cm/s (with ring characteristics $D = 5.83$ cm, $Re = 11\,100$, and $\tau = 0.153$ s). The dotted lines indicate the radial region for which the threshold condition $\bar{u}_b/\hat{u}_{b,c} \geq 1$ is satisfied. These data correspond to that shown in Figs. 3 and 4.

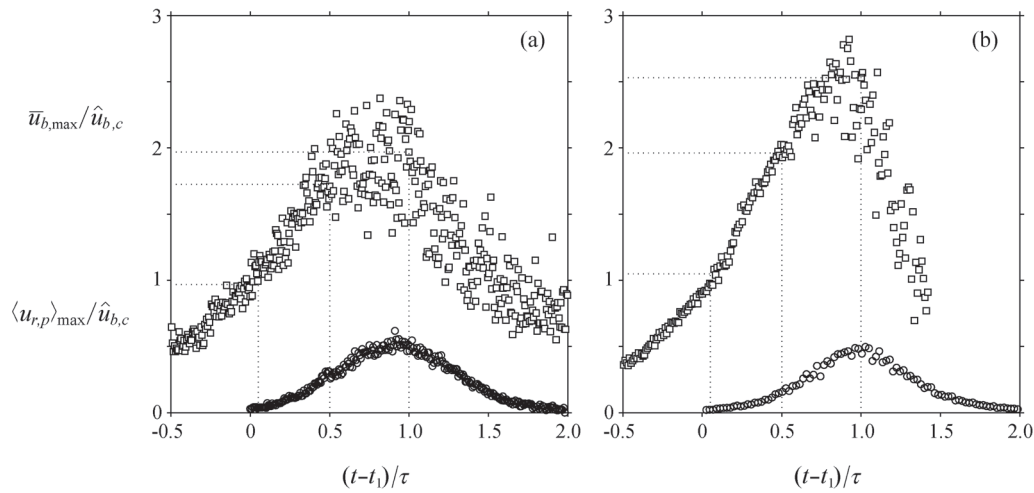


FIG. 8. Measured values of $\bar{u}_{b,\max}/\hat{u}_{b,c}$ (\square) and $\langle u_{r,p} \rangle_{\max}/\hat{u}_{b,c}$ (\circ) plotted against dimensionless time, $(t - t_0)/\tau$, for (a) $N/N_c = 5.92$ (type I, with $\hat{u}_{b,c} = 4.31$ cm/s, $\tau = 0.479$ s) and (b) $N/N_c = 7.95$ (type K, with $\hat{u}_{b,c} = 15.3$ cm/s, $\tau = 0.153$ s). The dotted lines indicate the times shown in Figs. 6 and 7.

of $\bar{u}_b(r, t)$ and $\langle u_{r,p} \rangle(r, t)$ remain aligned (radially) throughout the interaction and attain overall peak values at time $(t - t_1)/\tau \approx 1$, when the ring core is at its closest point to the bed surface.

For $(t - t_1)/\tau \gtrsim 1$, the vortex ring is rebounded away from the bed surface (as illustrated by Fig. 5). The reversal in direction of the ring's trajectory means that the magnitudes of $\bar{u}_b(r, t)$ and, hence, $\langle u_{r,p} \rangle(r, t)$ decrease uniformly during this period. This is best illustrated by Fig. 8, which shows the instantaneous peak values of $\bar{u}_b(r, t)$ and $\langle u_{r,p} \rangle(r, t)$, denoted, respectively, by $\bar{u}_{b,\max}$ and $\langle u_{r,p} \rangle_{\max}$, at each time during the interaction. As already noted, during the period $0 \leq (t - t_1)/\tau \leq 1$, $\langle u_{r,p} \rangle_{\max}$ and $\bar{u}_{b,\max}$ ($> \hat{u}_{b,c}$) increase uniformly as the ring core approaches the bed surface, attaining overall peak values when the core is closest to the bed. However, for $1 \leq (t - t_1)/\tau \leq 2$, $\langle u_{r,p} \rangle_{\max}$ and $\bar{u}_{b,\max}$ decrease uniformly as the vortex ring is rebounded. Note that $\langle u_{r,p} \rangle_{\max}$ increases from zero to attain its peak value over a period $\tau = D/2U$, and then decays back to zero over the same duration. At $(t - t_1)/\tau \approx 2$, the vortex structure breaks down, and so, no sediment motion is observed after this time.

It is also useful to compare Fig. 7 with the data in Fig. 3, which shows how the displaced sediment grains move, predominantly, along radial trajectories in the region below the core, with no (transverse) motion induced at the centre of the impact, below the axial stagnation point (at $x = 0$, $y = 0$). Munro *et al.*¹⁰ showed that the displaced grains slide, roll, or bounce over the undisturbed bed material below, eventually forming into a circular mound in the region beyond the instantaneous ring radius, where $\bar{u}_b(r, t)/\hat{u}_{b,c} \leq 1$ [for example, in Fig. 7(b) this will occur around $r/D \approx 0.8$]. Note that the diameter of the mound structure increases as the ring radius is stretched. The reader is referred to Sec. III (and Figs. 7–10) of Munro *et al.*¹⁰ for a detailed discussion and illustration of the mound formation.

The underlying interaction characteristics described above also apply to impacts under critical conditions ($N/N_c = 1$). However, the key difference for the $N/N_c = 1$ case is that grain motion occurs only at time $(t - t_1)/\tau \approx 1$ (when the ring core is at its closest point to the bed) and only in the region below the instantaneous core position, where $\bar{u}_b(r, t)$ has attained its overall peak value ($\hat{u}_{b,c}$). Unlike the cases shown in Figs. 3, 6, and 7, where the grains are displaced over a sustained period $2\tau = D/U$, the grain motion observed under critical impact conditions is instantaneous and occurs only for the brief moment when the threshold condition $\bar{u}_{b,\max}/\hat{u}_{b,c} = 1$ is satisfied. Note that, the values of $\hat{u}_{b,c}$ were measured directly from the fluid velocity data obtained from the $N/N_c = 1$ impacts. Recall, each of these experiments was repeated several times, and the $\hat{u}_{b,c}$ reported here are the corresponding average values (which had maximum variability within $\pm 7\%$). Figures 6 and

7 also show that the $\hat{u}_{b,c}$ remain a reliable measure of the threshold velocity for impact conditions with $N/N_c > 1$.

For the interactions described in this article (with $1 \leq N/N_c \leq 8$), the near-bed vertical fluid velocity component $\bar{w}_b(r, t)$ (indicated in Figs. 6 and 7 by the dash-dotted lines) has negligible effect on how the grains are displaced, during the period $0 \leq (t - t_1)/\tau \leq 1$. [This is not necessarily the case for more energetic impacts, where the vortex ring can cause significant erosion and penetrate further into the bed structure.]¹⁰ However, $\bar{w}_b(r, t)$ does play a crucial role in how the sediment is resuspended above the impact region. This typically occurs for $(t - t_1)/\tau \gtrsim 1$, as the ring is stretched and the outer streamlines of the ring structure approach the bed surface, which gives rise to a region of significant $\bar{w}_b > 0$, around $r/D \approx 0.8$ [see Figs. 6(c) and 7(c)]. During the impact, and provided the necessary conditions are satisfied (typically, $N/N_c \gtrsim 3$), displaced grains can become resuspended (or entrained) within the streamlines adjacent to the bed surface. This entrained material is advected around the streamline and into the $\bar{w}_b > 0$ region, whereupon the sediment is advected up into the outer fluid above the bed to form a distinctive axisymmetric “splash” of sediment. Evidence of this resuspension mechanism can be seen, to some extent, in Fig. 5. However, the reader is directed to Fig. 3 of Munro *et al.*¹⁰ for a clear and more detailed illustration of this process.

B. Critical conditions for sediment movement

The measured values of N_c are now presented. First, attention is focussed on the horizontal-bed case ($\beta = 0$), henceforth denoted by $N_{c,0}$. Using dimensional analysis, Shields¹ proposed a relationship between the critical Shields parameter and the boundary Reynolds number $Re_* = u_{*,c} d_p / \nu$, which has since largely been verified by experimental data obtained in steady turbulent channel flows.^{2–4,15} As already noted, the critical bed shear velocity $u_{*,c}$ (and hence Re_*) was not measured in the experiments reported here. However, in the region below the ring core, we expect the depth of the boundary layer established adjacent to the bed surface to be approximately $D/Re^{1/2}$. Likewise, the inner viscous sublayer in this region will have thickness of order $\delta_s = (D/Re)$.¹⁰ Therefore, under critical conditions, the hydrodynamic drag and lift forces acting on the near-surface sediment grains will depend on z^*/δ_s , where z^* is the (bed) roughness length scale, which will be $\mathcal{O}(d_p)$. Hence, for the experiments reported here, we expect $N_{c,0} = f(Re_p, d_p/\delta_s)$, where $d_p/\delta_s = U d_p / \nu$.³² Figure 9 shows the values of $N_{c,0}$ plotted against Re_p and d_p/δ_s , for each of the eleven sediment types. Separate data symbols have been used to differentiate between Diakon ($s = 1.2$) and Ballotini ($s = 2.5$) sediments. The error bars for $N_{c,0}$, Re_p , and d_p/δ_s are based on the typical variability of d_p , $\hat{u}_{b,c}$, w_s , and U .

The $N_{c,0}$ reported in Fig. 9 are two orders of magnitude larger than the traditional values obtained from studies using steady turbulent channel flows,^{1–4,15} and so, a direct quantitative comparison is precluded. However, a number of qualitative consistencies can be identified. In particular, White³ classified bedforms, under threshold conditions, as (hydraulically) smooth or rough. For the experiments considered here, a hydraulically rough bedform corresponds to when the roughness length scale (z^*) is comparable to (or larger than) the boundary-layer depth, and so, the surface sediment grains are exposed to hydrodynamic drag (F_D) and lift (F_L) forces that are $\mathcal{O}(\rho \hat{u}_{b,c}^2 d_p^2)$. For a hydraulically smooth bedform, z^* is significantly smaller than the boundary-layer depth, allowing a laminar viscous sublayer to be established in the fluid immediately above the bed surface, within which viscous stresses act to significantly reduce the drag and lift forces acting on exposed surface sediment. That is, when z^* is comparable to (or smaller than) the viscous-sublayer thickness δ_s , the surface sediment grains are exposed to velocities $\mathcal{O}(u_{b,c} z^*/\delta_s)$,¹⁷ and so, the drag and lift forces are $\mathcal{O}(\rho \epsilon^2 \hat{u}_{b,c}^4 d_p^4 / \nu^2)$,^{33,34} where $\hat{u}_{b,c}/U = \mathcal{O}(1)$ has been used, and $\epsilon = z^*/d_p$ (where $0 < \epsilon \leq 1$). The data reported by White³ (and other studies)^{2,15,16} suggest that hydraulically smooth bedforms correspond to $Re_* \lesssim 10$ (typically, $d_p \lesssim 200\text{--}300\ \mu\text{m}$ for natural sediments),³ for which case the critical Shields parameter is found to increase significantly with decreasing Re_* , due to the damping effect of the viscous sublayer. Conversely, when $Re_* \gtrsim 10$, this viscous damping effect ceases to be evident and the critical Shields parameter is found to vary very little with Re_* [and is constant for $Re_* \gtrsim 100$ i.e., $d_p \gtrsim 3\ \text{mm}$ for natural sediments)].¹⁶ Despite general scatter, a similar pattern can be identified in the data reported in Fig. 9. That is, for $d_p/\delta_s \lesssim 20$ ($Re_p \lesssim 20$) the measured

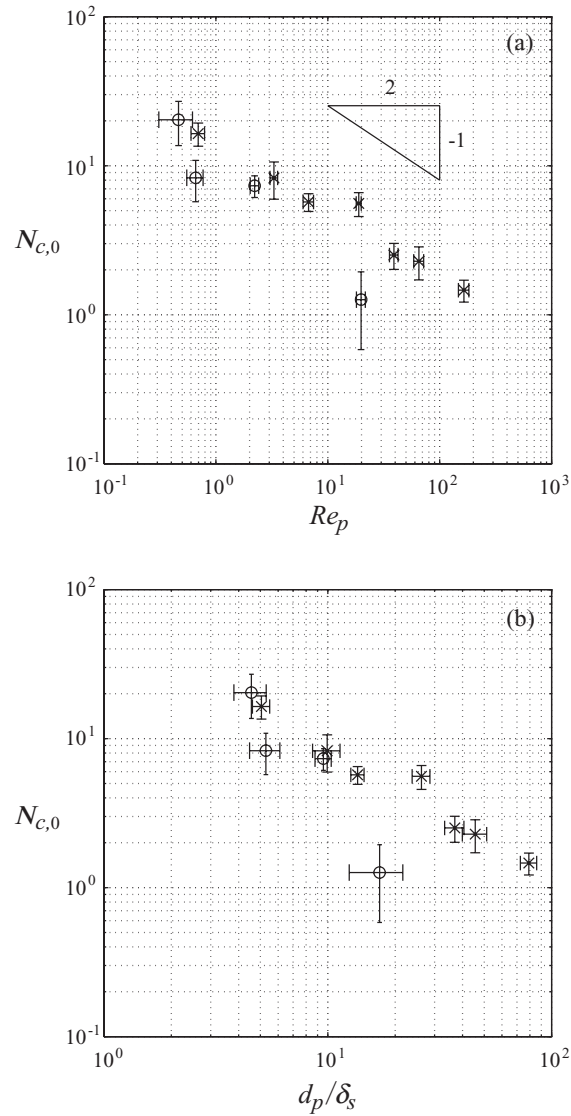


FIG. 9. Measured values of $N_{c,0}$ (\circ , Diakon; \times , Ballotini) plotted against (a) Re_p and (b) $d_p/\delta_s = Ud_p/\nu$. The slope of the solid-line triangle in (a) shows $N_{c,0} \sim Re_p^{-1/2}$.

values of $N_{c,0}$ increase monotonically with decreasing d_p/δ_s , whereas for $d_p/\delta_s \gtrsim 30$, $N_{c,0} \approx 2$ (and near-constant), which suggests that, here, the viscous damping effect becomes significant for $d_p/\delta_s \lesssim 20$ (which corresponds to $d_p \lesssim 350 \mu\text{m}$). Also note that in Fig. 9, $N_{c,0} \approx 11$ for the finest sediment, whereas $N_{c,0} \approx 2$ for the larger grain sizes. This factor of five difference is the same as that reported in White³ (for comparable grain sizes).

Furthermore, under threshold conditions (with $\beta = 0$), incipient grain motion occurs when the drag force (F_D) overcomes the net frictional force $\lambda_c(W - F_L)$ acting on the grain, where λ_c denotes the friction coefficient between grains and $W = \pi(s - 1)\rho g d_p^3/6$ is the grain's submerged weight. Hence, for hydraulically rough bedforms, the above condition reduces to $N_{c,0} \sim \mathcal{O}(1)$ (and constant). However, when $z^*/\delta_s \lesssim 1$ and the bedform is hydraulically smooth, the corresponding condition gives $N_{c,0} \sim \nu/\epsilon[(s - 1)gd_p^3]^{1/2}$, so that $N_{c,0}$ is dependent on the grain size (and density). Moreover, for sediment grains for which Stokes' Law,³⁵ $w_s = 2(s - 1)gd_p^2/9\nu$, is valid, this condition reduces to $N_{c,0} \sim Re_p^{-1/2}$. Again, the data in Fig. 9 display consistency with this description. In particular, the measured values of $N_{c,0}$ for $Re_p \lesssim 10$ show reasonable agreement with $N_{c,0} \sim Re_p^{-1/2}$, which is

shown in Fig. 9(a) by the slope of the solid-line triangle. Finally, note that, for fine-grained sediments, cohesive forces can become dominant in comparison with the grain weight. However, this situation occurs only for very fine particles with $d_p \lesssim 30 \mu\text{m}$,³⁶ considerably smaller than the grain sizes used here. Hence, here, the effects of cohesion have been ignored throughout.

We now consider how the measured values of N_c were affected by systematic increases in bed slope, relative to $\beta = 0$. The data are compared with a force-balance model,^{17,20} based on the required condition for incipient sediment motion on a sloping bed. Previous bed-slope studies have used this approach, but focussed exclusively on hydraulically rough bedforms (with $d_p \gtrsim 500 \mu\text{m}$).^{16,20} However, for the sediment types used here, the damping effect of the viscous sublayer also needs to be considered, and so, the force-balance model is re-derived to account separately for hydraulically rough and hydraulically smooth bedforms.

Consider a planar bedform consisting of cohesionless, monodisperse sediment, which is inclined with bed slope $\beta = \tan \phi$ (where $0 \leq \phi \leq \phi_r$). Using the notation introduced above, incipient motion of a surface sediment grain (in the down-slope direction) occurs when the force balance

$$F_D + W \sin \phi = \lambda_c (W \cos \phi - F_L) \quad (6)$$

is satisfied. Note that, in the absence of flow ($F_D = 0$, $F_L = 0$), incipient motion occurs only when the bed slope is at the repose limit, $\beta_r = \tan \phi_r$. Applying these conditions in Eq. (6) gives

$$\lambda_c = \tan \phi_r \equiv \beta_r. \quad (7)$$

Assuming that cohesive forces are negligible and that the sediment grains are spherical, the forces W , F_D , and F_L can be written in the form

$$W = \pi(s-1)\rho g d_p^3/6, \quad (8a)$$

$$(F_D, F_L) = \begin{cases} \pi(C_D, C_L)\rho\epsilon^2\hat{u}_{b,c}^4 d_p^4/2v^2 & \text{(smooth beds),} \\ \pi(C'_D, C'_L)\rho\hat{u}_{b,c}^2 d_p^2/2 & \text{(rough beds),} \end{cases} \quad (8b)$$

$$(8c)$$

where C_D , C'_D , C_L , and C'_L are drag and lift coefficients, which are dependent on Re_p and Re . Note that Re depends implicitly on bed slope β (i.e., an increase in β will typically result in a decrease in the ring propagation speed, U , required to induce incipient grain motion). Hence, in general, the drag and lift coefficients depend implicitly on β . Substituting Eqs. (7) and (8) into Eq. (6) and rearranging [using the definition of N_c given in Eq. (4)] gives

$$N_c = \begin{cases} \left[\frac{Qv^2}{\epsilon^2(s-1)gd_p^3} \left(1 - \frac{\beta}{\beta_r}\right) \cos \phi \right]^{1/2} & \text{(smooth beds),} \\ Q' \left(1 - \frac{\beta}{\beta_r}\right) \cos \phi & \text{(rough beds),} \end{cases} \quad (9a)$$

$$(9b)$$

where the coefficients Q and Q' are given by

$$Q = \beta_r/3(C_D + \beta_r C_L), \quad (10a)$$

$$Q' = \beta_r/3(C'_D + \beta_r C'_L). \quad (10b)$$

Note that, through their dependence on the drag and lift coefficients, Q and Q' are, in general, implicitly dependent on β . For a horizontal bed ($\phi = 0$, $\beta = 0$), Eq. (9) reduces to

$$N_{c,0} = \begin{cases} \left[\frac{Q_0 v^2}{\epsilon^2(s-1)gd_p^3} \right]^{1/2} & \text{(smooth beds),} \\ Q'_0 & \text{(rough beds),} \end{cases} \quad (11a)$$

$$(11b)$$

where Q_0 and Q'_0 are henceforth used to denote the respective values of Q and Q' when $\beta = 0$. Then, noting that $N_c/N_{c,0} = \hat{u}_{b,c}^2/\hat{u}_{b,c,0}^2$, Eqs. (9) and (11) can be combined to give

$$\frac{\hat{u}_{b,c}}{\hat{u}_{b,c,0}} = \begin{cases} \left[\frac{Q}{Q_0} \left(1 - \frac{\beta}{\beta_r} \right) \cos \phi \right]^{1/4} & \text{(smooth beds),} \\ \left[\frac{Q'}{Q'_0} \left(1 - \frac{\beta}{\beta_r} \right) \cos \phi \right]^{1/2} & \text{(rough beds),} \end{cases} \quad (12a)$$

where $\hat{u}_{b,c,0}$ denotes the value of $\hat{u}_{b,c}$ when $\beta = 0$. Equation (12b) is a generalised form of the expression derived and used in previous studies.^{16–20} In both cases, Eq. (12) predicts that the bedform becomes more mobile as the bed slope is increased, with $\hat{u}_{b,c}/\hat{u}_{b,c,0} \rightarrow 0$ as $\beta/\beta_r \rightarrow 1$ (and $\phi/\phi_r \rightarrow 1$). Comparing Eqs. (12a) and (12b) shows that the effective bed roughness can have a significant effect. That is, the damping due to the viscous sublayer acts as a stabilizing influence for smooth beds, reducing the rate at which the bed mobility increases with bed slope.

In general, one would expect the coefficients Q/Q_0 and Q'/Q'_0 to depend on Re_p and, implicitly, on β (via the implicit dependence of Re on β). However, the approximation $Q'/Q'_0 = 1$ has been used previously when applying Eq. (12b), which implies that $Q' = Q'(Re_p)$ and is unaffected by changes to the required critical flow conditions that arise when the bed slope is altered (between $0 \leq \beta \leq \beta_r$). Previous studies have shown that Eq. (12b), with $Q'/Q'_0 = 1$ assumed, is consistent with experimental data (using hydraulically rough bedforms).^{19,20,37} In particular, Chiew and Parker,²⁰ using natural sediments with d_p between 500 and 2700 μm and streamwise bed slopes in the range $0 \leq \beta/\beta_r \leq 0.85$, found good agreement with measurements of $u_{*,c}/u_{*,c,0}$ obtained from a steady closed-conduit flow, where the critical bed shear velocity ($u_{*,c}$) was estimated using a standard empirical formulation based on the streamwise time-averaged mean flow velocity.

Figure 10 shows the measured values of $\hat{u}_{b,c}/\hat{u}_{b,c,0}$ plotted against β/β_r , with each sediment type indicated by a different data symbol (see caption). Equations (12a) and (12b), with $Q/Q_0 = 1$ and $Q'/Q'_0 = 1$ assumed, have been included for comparison and are shown, respectively, by the solid-line and broken-line curves. For each curve, $\beta_r = \tan \phi_r$ was calculated using $\phi_r = 26.6^\circ$, which is the average value of the eleven repose angles reported in Table I. To prevent saturation,

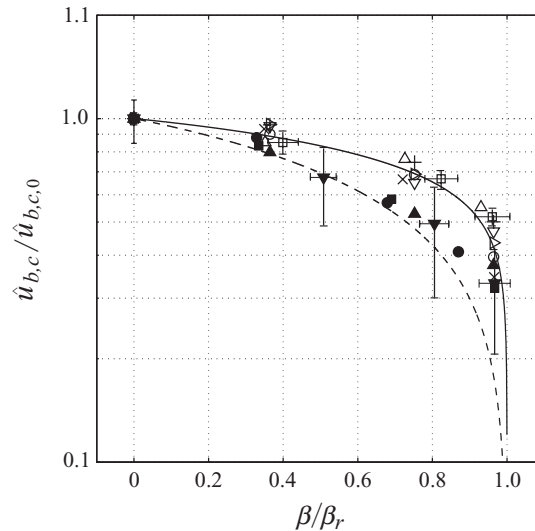


FIG. 10. Measured values of $\hat{u}_{b,c}/\hat{u}_{b,c,0}$ plotted against β/β_r for each of the eleven sediment types: A (\square), B (\circ), C (\triangle), D (∇), E ($+$), F (\times), G (\triangleright), H (\blacktriangle), I (\blacktriangledown), J (\blacksquare) and K (\bullet). [Here, the four solid black symbols have been used to denote the sediment types corresponding to hydraulically rough bedforms.] Equation (12a) (with $Q/Q_0 = 1$ assumed) is shown by the solid-line curve. Equation (12b) (with $Q'/Q'_0 = 1$ assumed) is shown by the broken-line curve. Error bars are shown for sediment types A and I.

TABLE II. A summary of the data presented in Figs. 9 and 10 (listed in order of increasing grain diameter, d_p).

Sediment type	d_p [μm]	s	Re_p	ϕ_r [deg]	ϕ [deg]	$\hat{u}_{b,c}$ [cm/s]	β/β_r	N_c	d_p/δ_s
A	80	2.5	0.696	24	0	13.9	0.00	16.4	5.06
					10	11.8	0.396	11.9	4.51
					20	9.28	0.818	7.32	3.38
					23	7.20	0.953	4.40	3.20
B	119	1.2	0.464	26	0	6.89	0.00	20.4	4.56
					10	6.21	0.362	16.5	4.16
					20	4.73	0.746	9.59	2.96
					25	2.73	0.956	3.19	1.48
C	157	1.2	0.659	27	0	5.06	0.00	8.30	5.29
					10	4.31	0.346	6.04	4.84
					20	3.86	0.714	4.83	3.78
					25	2.79	0.915	2.53	2.92
D	153	2.5	3.30	26	0	13.7	0.00	8.28	9.95
					10	13.0	0.362	7.48	9.03
					20	8.87	0.746	3.50	7.99
					25	6.41	0.956	1.83	7.01
E	220	2.5	6.73	26	0	13.6	0.00	5.71	13.6
					10	13.0	0.362	5.25	11.9
					20	10.1	0.746	3.18	10.6
					25	6.80	0.956	1.43	8.32
F	274	1.2	2.22	27	0	6.28	0.00	7.34	9.56
					10	5.86	0.346	6.39	8.03
					20	4.18	0.714	3.25	6.03
					26	2.17	0.957	0.876	4.25
G	374	2.5	18.9	26	0	17.5	0.00	5.58	26.2
					10	16.9	0.362	5.17	25.2
					20	12.1	0.746	2.65	19.6
					25	7.63	0.956	1.06	11.4
H	563	2.5	39.0	26	0	14.4	0.00	2.51	36.9
					10	11.5	0.362	1.60	29.3
					20	7.62	0.746	0.701	20.4
					25	5.41	0.956	0.353	13.2
I	751	1.2	19.8	28	0	4.31	0.00	1.26	17.0
					15	2.91	0.504	0.574	12.8
					23	2.13	0.798	0.309	12.3
					27	1.43	0.958	0.139	9.76
J	709	2.5	65.2	28	0	15.4	0.00	2.28	45.6
					10	12.8	0.332	1.58	41.4
					20	9.00	0.685	0.776	29.3
					27	4.96	0.958	0.235	16.7
K	1087	2.5	165.0	29	0	15.3	0.00	1.46	79.1
					10	13.5	0.318	1.13	63.6
					20	8.70	0.657	0.473	39.8
					25	6.26	0.841	0.245	26.4

error bars have been included for sediment type A (which are largely representative) and type I (which exhibit the largest degree of variability). To further aid the reader, the data presented in Fig. 10 are also tabulated in Table II, together with the corresponding values of d_p/δ_s . In particular, note that for each sediment type the values of $d_p/\delta_s = Ud_p/\nu$ decrease (i.e., $\delta_s = \nu/U$ increases) as the bed slope β is increased. The values of $\hat{u}_{b,c}/\hat{u}_{b,c,0}$ shown in Fig. 10 are well described by Eq. (12), either falling on or in the “transition” region between the two predicted trends. Furthermore, recall that the values of $N_{c,0}$ reported in Fig. 9 suggest that for the sediment types used here, the

transition to smooth-bed behaviour (where the effects of viscous damping are dominant) corresponds to $d_p/\delta_s \lesssim 20$. This property is further supported by the data in Fig. 10. Consider first the data for sediment types A–G, which are indicated by the open or crossed data symbols (see caption). Over the range of bed slopes considered here ($0 \leq \beta/\beta_r \leq 0.95$), the data for these sediment types satisfy $1.47 \leq d_p/\delta_s \leq 26.2$ (see Table II), and the corresponding values of $\hat{u}_{b,c}/\hat{u}_{b,c,0}$ shown in Fig. 10 are well described by the trend predicted in Eq. (12a). Moreover, these values of $\hat{u}_{b,c}/\hat{u}_{b,c,0}$ appear to be independent of grain size (within the level of general scatter), which supports the validity of the $Q/Q_0 = 1$ assumption (suggested by previous studies). Now consider the data for the larger sediment types H–K, which are shown in Fig. 10 by the solid black data symbols. The data for sediment types H, J, and K all satisfy $13.2 \leq d_p/\delta_s \leq 79.1$ (see Table II). Moreover, the measured values of $\hat{u}_{b,c}/\hat{u}_{b,c,0}$ corresponding to $d_p/\delta_s \gtrsim 20$ agree with the trend predicted by Eq. (12b) (and with the $Q'/Q'_0 = 1$ assumption). However, the values of $\hat{u}_{b,c}/\hat{u}_{b,c,0}$ satisfying $d_p/\delta_s \lesssim 20$, either fall in the region between the two curves, or are better described by Eq. (12a). As illustrated by Fig. 10, this departure from Eq. (12b) typically occurs when the bed slope has increased beyond $\beta/\beta_r \approx 0.85$. Hence, for these sediment types, the data suggest that as the bed slope approaches the repose limit, the corresponding decrease in effective bed roughness z^*/δ_s is sufficient to alter the behaviour of the bedform from hydraulically rough, to hydraulically smooth. [This is a further illustration, as noted in Lamb *et al.*,¹⁶ of the important role played by the effective bed roughness in controlling the critical criteria of incipient grain motion for sloped bedforms.]

Note that, for sediment type I (with $d_p = 751 \mu\text{m}$ and indicated by \blacktriangledown), the data satisfy $9.76 \leq d_p/\delta_s \leq 17.0$ over the range of bed slopes considered here. The corresponding values of $\hat{u}_{b,c}/\hat{u}_{b,c,0}$ either fall on the trend predicted by Eq. (12b), or in the transition region between the two curves. The reason for this is not known. However, it is worth reiterating that these data exhibit, by far, the largest degree of uncertainty.

IV. SUMMARY AND FINAL REMARKS

The experiments reported here examined the interaction between a vortex ring and a sloping (planar) sediment layer, with attention focussed on how the conditions for incipient sediment motion (in terms of the critical Shields parameter, N_c) were affected by systematic increases in bed slope. Since $u_{*,c}$ was not measured in these experiments, N_c was defined in terms of the peak tangential fluid velocity measured adjacent to the bed surface. Previous bed-slope studies used data obtained in steady turbulent channel (or conduit) flows, and focussed exclusively on hydraulically rough bedforms (typically with $d_p \gtrsim 500 \mu\text{m}$), and bed slopes between $0 \leq \beta/\beta_r \lesssim 0.8$.^{16,20} Here, this analysis was extended to consider hydraulically smooth beds (using sediments with d_p in the range 80 to $1087 \mu\text{m}$) and bed slopes $0 \leq \beta/\beta_r \leq 0.95$.

The measured values of $N_{c,0}$ (corresponding to $\beta = 0$) were compared with traditional measurements of the critical Shields parameter obtained in turbulent channel flows.^{1–4,15} Although notably different in magnitude, a similar qualitative trend was identified. In particular, the values of $N_{c,0}$ reported here suggest that the threshold for hydraulically smooth bedforms to be $d_p/\delta_s \approx 20$ (which corresponds to $d_p \sim 350 \mu\text{m}$). Below this threshold, the bed roughness (z^*) is comparable to (or smaller than) the viscous-sublayer thickness, and so, viscous stresses act to significantly reduce the hydrodynamic drag and lift forces acting on the near-surface sediment grains. Consequently, for $d_p/\delta_s \lesssim 20$, the measured values of $N_{c,0}$ were observed to increase monotonically with decreasing d_p/δ_s . For $d_p/\delta_s \gtrsim 30$, the effects of viscous damping cease to be evident, with little variation observed in the measured values of $N_{c,0}$. These observations are consistent with smooth-bedform threshold $Re^* \approx 10$ (corresponding to $d_p \approx 200\text{--}300 \mu\text{m}$) identified by previous studies.³

The data reported here show that bed slope has a significant influence on the threshold condition for sediment motion, with the bed becoming more mobile with increasing bed slope, due to the additional downslope gravitational force. The measured values of N_c , obtained for bed slopes $0 \leq \beta/\beta_r \leq 0.95$, were compared with a simple force-balance model, based on the required condition for incipient grain motion on a sloping bed. The standard derivation of this model, corresponding to hydraulically rough bedforms, takes the form given in Eq. (12b).¹⁷ Here, the model was extended to account for the case of hydraulically smooth beds. That is, for $z^*/\delta_s \lesssim 1$, the near-surface sediment

grains are exposed to reduced drag and lift forces, which here are assumed $\mathcal{O}(\rho \epsilon^2 u_{b,c}^4 d_p^4 / \nu^2)$.^{33,34} In this case, the corresponding model takes the form given in Eq. (12a). Comparing Eqs. (12a) and (12b) shows that the damping effect of the viscous sublayer acts as a stabilizing mechanism for smooth beds, reducing the rate at which the bed mobility increases with bed slope. The measured values of $u_{b,c}/u_{b,c,0} = (N_c/N_{c,0})^{1/2}$ were consistent with Eq. (12), either falling on, or in the region between, the two predicted trends. Moreover, the data show a transition in behaviour between the smooth-bed and rough-bed cases when $d_p/\delta_s \approx 20$ (in agreement with the threshold identified for the $N_{c,0}$ data).

The basis of the arguments used to derive Eq. (12a) is not unique to the interaction considered in this article and are expected to apply also to fully turbulent flows. That is, for a steady turbulent channel flow, it is known the viscous sublayer has an average thickness $\delta_s = 11.6u_*/\nu$ and that the threshold for hydraulically smooth beds corresponds to $Re_* \approx 10$.¹⁷ Hence, for $z_*/\delta_s \lesssim 1$, one expects the surface sediment grains to be exposed to reduced velocities $\mathcal{O}(u_*^2 z_*/\nu)$, and so to drag and lift forces $\mathcal{O}(\rho \epsilon^2 u_*^4 d_p^4 / \nu^2)$ (where, as before, $\epsilon = z_*/d_p$). In this case, the corresponding force balance will be equivalent to the form given in Eq. (12a). Of course, the characteristics of the interaction described in this article are notably different from those associated with the coherent structures observed in turbulent channel flows,^{8,12} and are more readily associated with turbulence in the absence of a mean flow. A detailed study, using zero-mean turbulence generated by a steadily oscillating grid, is currently being undertaken to further investigate the role played by coherent structures (and turbulent fluctuations) in the sediment transport process. In particular, this study will analyse the effects of bed slope on the critical criteria for incipient sediment motion, and the validity of Eqs. (12a) and (12b).

ACKNOWLEDGMENTS

This work was funded by the Engineering and Physical Sciences Research Council (Grant No. EP/H007032/1). The author gratefully acknowledges Wan Hanna Melini Wan Mohtar, Ben Cooper-Smith, and Tom Shaw for assisting with the experiments, and the technical support provided by Damien Goy and Mike Langford.

- ¹ A. Shields, "Anwendung der Ähnlichkeitsmechanik und der turbulenzforschung auf die geschiebebewegung," *Preussische Versuchsansalt für Wasserbau und Schiffbau* **26**, 26 (1936).
- ² C. M. White, "The equilibrium of grains on the bed of a stream", *Proc. Roy Soc. London Ser. A* **174**, 322 (1940).
- ³ S. J. White, "Plane bed thresholds for fine grained sediments," *Nature (London)* **228**, 152 (1970).
- ⁴ J. R. D. Francis, "Experiments on the motion of solitary grains along the bed of a water-stream," *Proc. R. Soc. London, Ser. A* **332**, 443 (1973).
- ⁵ B. M. Sumer, L. H. C. Chua, N. S. Cheng, and J. Fredsøe, "The influence of turbulence on bedload sediment transport," *J. Hydraul. Eng.* **129**, 585 (2003).
- ⁶ J. M. Nelson, S. R. Mclean, and S. R. Wolfe, "Mean flow and turbulence fields over two-dimensional bed forms," *Water Resour. Res.* **29**, 3935 (1993).
- ⁷ J. M. Nelson, R. L. Shreve, S. R. Mclean, and T. G. Drake, "Role of near-bed turbulence structure in bed load transport and bed form mechanics," *Water Resour. Res.* **30**, 2071 (1995).
- ⁸ Y. Niño and M. H. Garcia, "Experiments on particle-turbulence interactions in the near-wall region of an open channel flow: Implications for sediment transport," *J. Fluid Mech.* **326**, 285 (1996).
- ⁹ B. Willets, "Aeolian and fluvial grain transport," *Philos. Trans. R. Soc. London, Ser. A* **356**, 2497 (1998).
- ¹⁰ R. J. Munro, N. Bethke, and S. B. Dalziel, "Sediment resuspension and erosion by vortex rings," *Phys. Fluids* **21**, 046601 (2009).
- ¹¹ R. J. Munro and S. B. Dalziel, "Attenuation technique for measuring sediment displacement levels," *Exp. Fluids* **39**, 600 (2005).
- ¹² D. Kaftori, G. Hetsroni, and S. Banerjee, "Particle behaviour in the turbulent boundary layer I. Motion, deposition and entrainment," *Phys. Fluids* **7**, 1095 (1995).
- ¹³ L. C. van Rijn, "Sediment transport, part I: Bed load transport," *J. Hydraul. Eng.* **110**(10), 1431 (1984).
- ¹⁴ S. Q. Yang and S. Y. Lim, "Total load transport formula for flow in alluvial channels," *J. Hydraul. Eng.* **129**(1), 68 (2003).
- ¹⁵ W. R. Brownlie, "Flow depth in sand-bed channels," *J. Hydraul. Eng.* **109**(7), 959 (1983).
- ¹⁶ M. P. Lamb, W. E. Dietrich, and J. G. Venditti, "Is the critical Shields stress for incipient sediment motion dependent on channel-bed slope," *J. Geophys. Res.* **113**, F02008, doi:10.1029/2007JF000831 (2008).
- ¹⁷ P. L. Wiberg and J. D. Smith, "Calculations of the critical shear stress for motion of uniform and heterogeneous sediments," *Water Resour. Res.* **23**(8), 1471 (1987).
- ¹⁸ E. R. Mueller, J. Pitlick, and J. Nelson, "Variation in the reference shields stress for bed load transport in gravel-bed streams and rivers," *Water Resour. Res.* **41**(4), W04006 (2005).

- ¹⁹ R. J. S. Whitehouse and J. Hardisty, "Experimental assessment of two theories for the effect of bed slope on the threshold of bedload transport," *Mar. Geol.* **79**, 135 (1988).
- ²⁰ Y.-M. Chiew and G. Parker, "Incipient sediment motion on non-horizontal slopes," *J. Hydraul. Res.* **32**, 649 (1994).
- ²¹ T. Maxworthy, "The structure and stability of vortex rings," *J. Fluid Mech.* **51**, 15 (1972).
- ²² P. F. Linden, "The interaction of a vortex ring with a sharp density interface: A model for turbulent entrainment," *J. Fluid Mech.* **60**, 467 (1973).
- ²³ W. J. A. Dahm, C. M. Scheil, and G. Tryggvason "Dynamics of a vortex ring interacting with a density interface," *J. Fluid Mech.* **205**, 1 (1989).
- ²⁴ P. G. Saffman, "Formation of vortex rings", *Studies in Applied Mathematics*, vol 54, issue 3, p 261–268 (1975), ISSN-0022-2526.
- ²⁵ R. J. Munro, S. B. Dalziel, and H. Jehan, "A pattern matching technique for measuring sediment displacement levels," *Exp. Fluids* **37**, 399 (2004).
- ²⁶ As of October, 2009, available at Dalziel Research Partners, 142 Cottenham Road, Histon, Cambridge CB24 9ET, UK.
- ²⁷ S. E. Widnall and J. P. Sullivan, "On the stability of vortex rings," *Proc. R. Soc. London, Ser. A* **332**, 335 (1973).
- ²⁸ J. J. Allen and B. Auvity, "Interaction of a vortex ring with a piston vortex," *J. Fluid Mech.* **465**, 353 (2002).
- ²⁹ J. D. A. Walker, C. R. Smith, A. W. Cerra, and T. L. Doligalski, "The impact of a vortex ring on a wall," *J. Fluid Mech.* **181**, 99 (1987).
- ³⁰ J. D. Swearingen, J. D. Crouch, and R. A. Handler, "Dynamics and stability of a vortex ring impacting a solid boundary," *J. Fluid Mech.* **297**, 1 (1995).
- ³¹ T. L. Doligalski, C. R. Smith, and J. D. A. Walker, "Vortex interactions with walls," *Annu. Rev. Fluid Mech.* **26**, 573 (1994).
- ³² Y. Niño, F. Lopez, and M. Garcia, "Threshold for particle entrainment into suspension," *Sedimentology* **50**, 247 (2003).
- ³³ G. P. Krishnan and D. T. Leighton, "Inertial lift on a moving sphere in contact with a plane wall in a shear flow," *Phys. Fluids* **7**, 2538 (1995).
- ³⁴ I. Eames and S. B. Dalziel, "Dust resuspension by the flow around an impacting sphere," *J. Fluid Mech.* **403**, 305 (2000).
- ³⁵ G. K. Batchelor, *An Introduction to Fluid Mechanics* (Cambridge University Press, Cambridge, England, 1967).
- ³⁶ M. Phillips, "A force balance model for particle entrainment into a fluid stream," *J. Phys. D: Appl. Phys.* **13**, 221 (1980).
- ³⁷ C. Ancey, F. Bigillon, P. Frey, J. Lanier, and R. Ducret, "Saltating motion of a bead in a rapid water stream," *Phys. Rev. E* **66**, 1 (2002).